230 GHz VLBI Observations of M87: Event-horizon-scale Structure during an Enhanced Very-high-energy γ-Ray State in 2012

Akiyama, K.; Lu, R.; Fish, V.L.; Doeleman, S.S.; Broderick, A.E.; Dexter, J.; ... ; Ziurys, L.M.

The Astrophysical Journal, 807:150 (11pp), 2015 July 10 doi:10.1088/0004-637X/807/2/150

230 GHz VLBI OBSERVATIONS OF M87: EVENT-HORIZON-SCALE STRUCTURE DURING AN ENHANCED VERY-HIGH-ENERGY γ-RAY STATE IN 2012

Kazunori Akiyama[1,2,22], Ru-Sen Lu[3,4], Vincent L. Fish[3], Sheperd S. Doeleman[3,5], Avery E. Broderick[6,7], Jason Dexter[8], Kazuhiro Hada[2,9], Motoki Kino[10], Hiroshi Nagai[2], Mareki Honma[2,11], Michael D. Johnson[5], Juan C. Algaba[10,12], Keiichi Asada[12], Christiaan Brinkerink[13], Ray Blundell[5], Geoffrey C. Bower[14], Roger Cappallo[3], Geoffrey B. Crew[3], Matt Dexter[15], Sergio A. Dzib[4,16], Robert Freund[17], Per Friberg[18], Mark Gurwell[5], Paul T. P. Ho[12], Makoto Inoue[12], Thomas P. Krichbaum[4], Laurent Loinard[16], David MacMahon[15], Daniel P. Marrone[17], James M. Moran[5], Masanori Nakamura[12], Neil M. Nagar[19], Gisela Ortiz-Leon[16], Richard Plambeck[15], Nicolas Pradel[12], Rurik A. Primiani[5], Alan E. E. Rogers[3], Alan L. Roy[4], Jason SooHoo[3], Jonathan-León Tavares[20], Remo P. J. Tilanus[13,21], Michael Titus[3], Jan Wagner[4,10], Jonathan Weintroub[5], Paul Yamaguchi[5], Ken H. Young[5], Anton Zensus[4], and Lucy M. Ziurys[17]

[1] Department of Astronomy, Graduate School of Science, The University of Tokyo, 7-3-1 Hongo, Bunkyo-ku, Tokyo 113-0033, Japan; kazunori.akiyama@nao.ac.jp
[2] National Astronomical Observatory of Japan, 2-21-1 Osawa, Mitaka, Tokyo 181-8588, Japan
[3] Massachusetts Institute of Technology, Haystack Observatory, Route 40, Westford, MA 01886, USA
[4] Max-Planck-Institut für Radioastronomie, Auf dem Hügel 69, D-53121 Bonn, Germany
[5] Harvard Smithsonian Center for Astrophysics, 60 Garden Street, Cambridge, MA 02138, USA
[6] Perimeter Institute for Theoretical Physics, 31 Caroline Street, North Waterloo, Ontario N2L 2Y5, Canada
[7] Department of Physics and Astronomy, University of Waterloo, 200 University Avenue West, Waterloo, Ontario N2l 3G1, Canada
[8] Max Planck Institute for Extraterrestrial Physics, Giessenbachstr. 1, D-85748 Garching, Germany
[9] INAF Istituto di Radioastronomia, via Gobetti 101, I-40129, Bologna, Italy
[10] Korea Astronomy and Space Science Institute (KASI), 776 Daedeokdae-ro, Yuseong-gu, Daejeon 305-348, Korea
[11] Graduate University for Advanced Studies, Mitaka, 2-21-1 Osawa, Mitaka, Tokyo 181-8588, Japan
[12] Institute of Astronomy and Astrophysics, Academia Sinica, P.O. Box 23-141, Taipei 10617, Taiwan
[13] Department of Astrophysics/IMAPP, Radboud University Nijmegen, P.O. Box 9010, 6500 GL Nijmegen, The Netherlands
[14] Academia Sinica Institute of Astronomy and Astrophysics, 645 N. Aóhoku Place, Hilo, HI 96720, USA
[15] Department of Astronomy, 501 Campbell Hall, University of California, Berkeley, CA 94720-3411, USA
[16] Centro de Radiostronomía y Astrofísica, Universidad Nacional Autónoma de México, Morelia 58089, Mexico
[17] Arizona Radio Observatory, Steward Observatory, University of Arizona, 933 North Cherry Avenue, Tucson, AZ 85721-0065, USA
[18] James Clerk Maxwell Telescope, Joint Astronomy Centre, 660 North Aóhoku Place, University Park, Hilo, HI 96720, USA
[19] Astronomy Department, Universidad de Concepción, Concepción, Chile
[20] Instituto Nacional de Astrofísica Óptica y Electrónica (INAOE), Apartado Postal 51 y 216, 72000 Puebla, Mexico
[21] Leiden Observatory, Leiden University, P.O. Box 9513, 2300 RA Leiden, The Netherlands
Received 2014 November 11; accepted 2015 May 13; published 2015 July 9

ABSTRACT

We report on 230 GHz (1.3 mm) very long baseline interferometry (VLBI) observations of M87 with the Event Horizon Telescope using antennas on Mauna Kea in Hawaii, Mt. Graham in Arizona, and Cedar Flat in California. For the first time, we have acquired 230 GHz VLBI interferometric phase information on M87 through measurement of the closure phase on the triangle of long baselines. Most of the measured closure phases are consistent with 0° as expected by physically motivated models for 230 GHz structure such as jet models and accretion disk models. The brightness temperature of the event-horizon-scale structure is $\sim 1 \times 10^{10}$ K derived from the compact flux density of ~1 Jy and the angular size of ~40 μas ~ 5.5 R_s, which is broadly consistent with the peak brightness of the radio cores at 1–86 GHz located within $\sim 10^2$ R_s. Our observations occurred in the middle of an enhancement in very-high-energy (VHE) γ-ray flux, presumably originating in the vicinity of the central black hole. Our measurements, combined with results of multi-wavelength observations, favor a scenario in which the VHE region has an extended size of ~20–60 R_s.

Key words: galaxies: active – galaxies: individual (M87) – galaxies: jets – radio continuum: galaxies – techniques: high angular resolution – techniques: interferometric

Supporting material: machine-readable tables

1. INTRODUCTION

Relativistic jets pose many intriguing questions in astrophysics related to their formation process and the production mechanism of high-energy particles and photons. The relativistic jet in the radio galaxy M87 is an excellent laboratory for investigating these issues; because of its proximity ($D = 16.7 \pm 0.6$ Mpc; Blakeslee et al. 2009) and the large estimated mass of its central black hole ($M_{BH} \sim (3-6) \times 10^9 M_\odot$; Macchetto et al. 1997; Gebhardt et al. 2011; Walsh et al. 2013), the black hole in M87 subtends the second largest angular size of any known black hole (after Sgr A*).

Millimeter/submillimeter-wavelength very long baseline interferometry (VLBI) is ideally suited to observing M87 on these scales, since the event-horizon-scale structure around the black hole is expected to become optically thin at $\nu \gtrsim 230$ GHz ($\lambda \lesssim 1.3$ mm), based on the frequency-dependent position of the radio core (Hada et al. 2011) and the existence of the submillimeter bump in its radio spectrum

[22] Research Fellow of the Japan Society for the Promotion of Science.

indicating the opacity transition at ~230 GHz (Doi et al. 2013).

The origin of the 230 GHz emission is still an unsettled question. The 230 GHz emission could be dominated by synchrotron emission from either the jet (Zakamska et al. 2008; Broderick & Loeb 2009; Gracia et al. 2009; Dexter et al. 2012) or the accretion disk (Reynolds et al. 1996; Di Matteo et al. 2003; Nagakura & Takahashi 2010; Takahashi & Mineshige 2011; Dexter et al. 2012) in the regime of radiatively inefficient accretion flow (e.g., Yuan & Narayan 2014) with low mass accretion rate of $<9.2 \times 10^{-4} M_{\odot}$ yr^{-1} (Kuo et al. 2014). The discovery of the position shift of the radio core along the jet direction at different frequencies (Hada et al. 2011) provides strong evidence that the jet emission dominates the emission from the radio core at frequencies at least lower than 43 GHz (=7 mm). However, it is less clear for 230 GHz emission, since the extrapolated location of the 230 GHz radio core coincides with the jet base and/or central black hole within its uncertainty, and thus emission from the accretion disk could dominate.

VLBI observations at such high frequencies ($\lambda \lesssim 1.3$ mm, $\nu \gtrsim 230$ GHz) have been technically challenging due to the limited sensitivity of the instruments, fast atmospheric phase fluctuations and the small number of stations available. Recent technical developments (e.g., phased-array processors, digital backends, and recording systems with broad bandwidths) and the addition of new (sub)millimeter telescopes have led to a breakthrough to (sub)millimeter VLBI observations. In particular, significant progress on 230 GHz VLBI observations has been achieved in the last few years with the Event Horizon Telescope (EHT; Doeleman et al. 2008, 2009, 2012; Fish et al. 2011, 2013; Lu et al. 2012, 2013, 2014).

Previous 230 GHz VLBI observations (Doeleman et al. 2012, hereafter D12) with the EHT established the existence of compact structures on scales of few Schwarzschild radii (R_s), broadly consistent with a paraboloidal or possibly conical collimation profile of the jet width in the innermost region within ~100 R_s of the central black hole (Asada & Nakamura 2012; Hada et al. 2013; Nakamura & Asada 2013). These are naturally explained by recent theoretical MHD schemes (e.g., McKinney 2006; Komissarov et al. 2007).

VLBI observations at 230 GHz can address at least two issues concerning the fundamental nature of M87. The first is the event-horizon-scale structure of the jet launching region, which is crucial for understanding the formation process of the relativistic jets and also for testing the presence of signatures of strong-field gravitational lensing. Geometric models including a shadow feature at the last photon orbit, illuminated by a counter jet and/or accretion disk in the close vicinity of the black hole, can be fit to current 230 GHz observations. These models produce a relatively dim central region encircled by a brighter annulus (e.g., Broderick & Loeb 2009; Dexter et al. 2012), which can be properly imaged as the number of (sub) millimeter VLBI sites increases (Honma et al. 2014; Inoue et al. 2014; Lu et al. 2014).

The second issue is the production mechanism of very-high-energy (VHE; $\gtrsim$100 GeV) γ-ray photons in the vicinity of the black hole and/or the jet base. M87 is one of only four known active galactic nuclei (AGNs) with weak or moderate beaming compared to other VHE AGNs, which mostly consist of BL Lac objects. M87 has undergone three large VHE flares (see Abramowski et al. 2012, for an overview) and a weak VHE enhancement recently in 2012 March (Beilicke & VERITAS Collaboration 2012). In the past three flares, the compact sizes of the VHE emission region ($<5 \times 10^{15} \delta$ cm corresponding to a few R_s, where δ is the Doppler factor of the emission region) are required by rapid variability timescales of ~1 day based on causality arguments. The VHE flares in 2008 and 2010 were followed by delayed strong and weak 43 GHz flux density enhancements, respectively, in the radio core at 43 GHz (Acciari et al. 2009; Hada et al. 2012), indicating that these flares originate inside the radio core at 43 GHz only a few tens of R_s downstream from the black hole and/or jet base (Hada et al. 2011).

On the other hand, a weak VHE enhancement in 2012 March (hereafter the 2012 event) has different properties to previous VHE flares. Its long duration (~2 months) and weak flux (~10 times weaker than the past three flares) may point to an origin in a different type of VHE activity. Multi-wavelength observations on milliarcsecond scales revealed strong enhancement in the radio core at both 22 and 43 GHz after the 2012 event, suggesting an origin close to the black hole and/or jet base, similar to the 2008 VHE flare (Hada et al. 2014, hereafter H14). In summary, three of four previous VHE events are thought to originate in the vicinity of the black hole. 230 GHz VLBI is the ideal tool to constrain the location and structure of the VHE emission region.

We report on new 230 GHz VLBI observations of M87 with the EHT during the 2012 event using a four-telescope array, providing the interferometric visibility information on baselines shorter than ~4 Gλ. These observations provide the first measurements of closure phase, imposing new constraints on accretion/jet models for M87, and the first constraints on the innermost structure of the relativistic jet on scales of a few R_s during VHE variability. In this paper, we adopt a black hole mass of $6.2 \times 10^9 M_{\odot}$[23] following Gebhardt et al. (2011) and a distance of 16.7 Mpc following Blakeslee et al. (2009) along with D12, resulting in $R_s = 1.9 \times 10^{15}$ cm $= 5.9 \times 10^{-4}$ pc $= 7.3$ μas.

Table 1
Observatories in the 2012 Observations

Site	Observatory	Char.	Note
Hawaii	SMA	P	Phased sum of seven 6 m dishes
Arizona	ARO/SMT	S	Single 10 m dish
California	CARMA (phased)	F	Phased sum of three 10.4 m and four 6.1 m dishes
California	CARMA (single)	D	Single 10.4 m dish

2. OBSERVATIONS

M87 and several calibrator sources were observed with four stations at three sites in 2012 on the nights of March 15, 20 and 21 (days 75, 80 and 81), as summarized in Table 1: a phased array of the Submillimeter Array (SMA; Ho et al. 2004; henceforth, P) antennas and the James Clerk Maxwell Telescope (JCMT; Newport 1986) on Mauna Kea in Hawaii, the Arizona Radio Observatory's Submillimeter Telescope (ARO/SMT; Martin & Baars 1986; S) on Mt. Graham in Arizona, and both a single antenna and a phased array of eight

[23] This black hole mass is recalculated for a distance of 16.7 Mpc.

antennas of the Combined Array for Research in Millimeter-wave Astronomy (CARMA; Mundy & Scott 2000; D and F, respectively) in Cedar Flat in California.

Observations were performed at two bands centered at 229.089 and 229.601 GHz (low and high band) with 480 MHz bandwidths with the exception of the single CARMA antenna, which observed only the low band. All telescopes observed left-hand circular polarization (LHCP). The SMT and phased CARMA, along with the JCMT on Mauna Kea, also observed right-hand circular polarization (RHCP). Hydrogen masers were used as timing and frequency references at all sites. Reconfigurable Open Architecture Computing Hardware (ROACH)[24] digital backends (RDBE) designed at MIT Haystack Observatory and NRAO were used for all single-antenna stations. Data were recorded onto modules of hard drives using the Mark 5C for RDBE systems. The SMA and CARMA sites were equipped with 1 GHz bandwidth adaptive beamformers, built using an older generation of Collaboration for Astronomy Signal Processing and Electronics Research[25] technology. The beamformers compensate group delay and phase at each antenna in the array in real time, thereby recording a single data stream representing the coherent phased-array sum of all antennas. The real-time corrections are derived from simultaneous cross-correlations, and the data are formatted for Mark 5B+ recorders at a rate of 4 Gb s^{-1}. Data were correlated with the Haystack Mark 4 VLBI correlator.

Hardware and disk failures occurred during observations on the first two days, with the result that many data products are missing or have low signal-to-noise ratio (S/N). The LHCP data of the first two days and RHCP data cannot be calibrated by the technique of amplitude self-calibration described below. In this paper, we focus on the results of LHCP data of M87 in day 81; other data will be presented elsewhere.

3. DATA REDUCTION

Correlated data were analyzed using the Haystack Observatory Post-processing System[26] (HOPS). Initial coherent baseline fringe fitting was done using the HOPS task `fourfit`. Detections with high S/N were used to determine several important quantities for further processing. First, we derived the phase offsets between the 32 MHz channels within each band. Second, approximate atmospheric coherence times maximizing the S/N of detection were calculated to guide further incoherent fringe searching in the HOPS task `cofit`. Third, the residual single-band delay, multi-band delay, and delay rate were used to set up narrow search windows for each source to assist in fringe finding.

A form of phase self-calibration was used to find fringes on baselines with low S/N, including long baselines (e.g., SP) and baselines including the single CARMA antenna. The phased CARMA station is very sensitive and therefore can be used as a reference station to derive phase corrections to be applied to other antennas to remove rapid atmospheric phase fluctuations through baselines with the phased CARMA station. The fringe fitting was done on baselines to station F (i.e., FD, SF, and PF), and data were segmented at a ~5 s cadence. These phases were then removed from each station prior to coherent fringe fitting on the low-S/N baselines using `fourfit`, leading to much better coherence and detections with higher S/N.

Detected fringes were segmented at a cadence of 1 s and incoherently averaged to produce estimates of the correlation coefficients not biased due to the noise and the coherence loss (Rogers et al. 1995). We confirmed that correlation coefficients derived with and without the phase-referencing technique were consistent, indicating that this phase-referencing technique does not bias our amplitude estimates. In addition, segmented bispectra were also formed at a 10 s cadence and averaged to construct scan-averaged estimates of the closure phase.

The visibilities were calibrated as in Lu et al. (2013; see also Fish et al. 2011; Lu et al. 2012). Visibilities were a priori calibrated by multiplying the VLBI correlation coefficient by the geometric mean of the system-equivalent flux density of the pair of antennas. Additional instrumental effects on the SMA were corrected (see Lu et al. 2013 for details). Finally, visibilities were amplitude self-calibrated assuming that the intra-site VLBI baseline at CARMA (FD) measures the same total flux density as the CARMA interferometer. In principle this assumption could be incorrect due to arcsecond-scale structure in the jet, which could produce the appearance of different correlated flux densities on different baselines within CARMA. However, M87 in 2012 March satisfies our assumption, as the arcsecond-scale jet was dominated by its unresolved (i.e., point-like) radio core, while the radio flux from extended components was $<1\%$ of the core flux. Thus, the VLBI amplitudes measured on the intra-site FD baseline should be consistent with the core flux density measured with CARMA as a connected array. For each scan, band, and site, gains were calculated for each station to maximize self-consistency of the visibilities, including consistency of the calibrated FD flux density with the total flux density measured by CARMA. Calibration errors of 5% have been added in quadrature to the random errors associated with the fringe search and estimation of the correlation coefficient on each baseline following previous observations (e.g., Fish et al. 2011; Lu et al. 2012). Note that we flagged data on scans when CARMA has a low phasing efficiency due to bad weather conditions, showing systematic losses in gain-calibrated amplitudes.

4. RESULTS

4.1. First Detections of Closure Phases of M87

We detected fringes on baselines to all three sites, consistent with the results of Doeleman et al. (2012). Furthermore, we detected closure phases on the Arizona–Hawaii–California triangle. Figure 1 shows the measured closure phase on the SPF/SPD triangles (upper; hereafter VLBI triangles) listed in Table 2 and SFD/PFD triangles (lower; hereafter trivial triangles). The average error bar on closure phases is $10\overset{\circ}{.}3$ for VLBI triangles and $5\overset{\circ}{.}0$ for trivial triangles. The error-weighted average of the closure phases by the square of S/N is $-0\overset{\circ}{.}7 \pm 2\overset{\circ}{.}9$ for VLBI triangles and $-0\overset{\circ}{.}1 \pm 0\overset{\circ}{.}6$ for trivial triangles. The closure phase is consistent with zero on trivial triangles, as would be expected if the source is point-like on arcsecond scales. All closure phases on VLBI triangles coincide with zero within the 1σ level except for one data point, which is consistent with zero within 2σ levels. We note that non-detections in VLBI triangles during 7:00–10:00 UTC are attributable to non-detections on the SP baseline (Figure 2).

[24] https://casper.berkeley.edu/wiki/ROACH
[25] https://casper.berkeley.edu
[26] http://www.haystack.mit.edu/tech/vlbi/hops.html

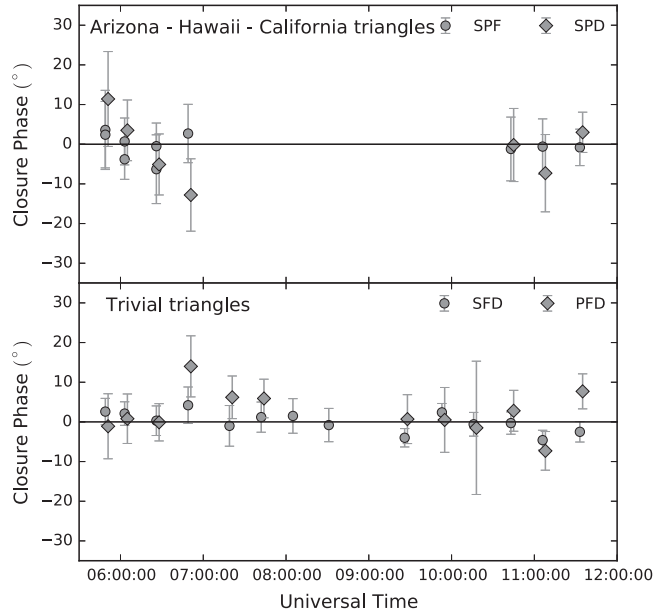

Figure 1. The measured closure phase of M87 as a function of time. Errors are 1σ. We added small offsets in UTC to each baseline data to avoid overlaps of error bars. Upper panel: the closure phase on AZ–CA–HI triangles. Lower panel: the closure phase on trivial triangles, which include an intra-site baseline in CARMA. The closure phase on the trivial triangle is expected to be zero.

4.2. The Geometrical Model of M87

The correlated flux density of M87 is shown in Figure 2 and Table 3. The arcsecond-scale core flux density of 2.2 Jy is ~17% higher than the 1.9 Jy measured in 2009 (D12). This brightening on arcsecond scales is not accompanied by changes on VLBI scales. The visibility amplitudes are broadly consistent with 2009 results of D12, confirming the presence of the event-horizon-scale structure. This indicates that the region responsible for the higher flux density must be resolved out in these observations and therefore located somewhere down the jet.

Most of the missing flux on VLBI scales is most likely attributed to the extended jet inside the arcsecond-scale radio core including the bright and stable knots such as HST-1. In the last decade, no radio enhancement was detected in such bright knots except for the 2005 VHE flare at HST-1. Even for the exceptionally variable HST-1, the radio flux has been decreasing from the 2005 VHE flare to at least the end of the 2012 event (see Abramowski et al. 2012 and H14). The observed increment in the missing flux seems incompatible with this trend in the bright knots, favoring that the missing flux originates in the vicinity of the radio core on milli-arcsecond scales rather than the bright knot features. We discuss it in a physical context related with the 2012 event in Section 5.3.

The structure of M87 is not yet uniquely constrained, since millimeter VLBI detections of M87 remain limited in terms of baseline length and orientation, similar to previous observations in D12. Even with our detections of closure phase, our small data set is consistent with a variety of geometrical models (see Section 5.1 for physically motivated models). It is still instructive to investigate single-Gaussian models, which inherently predict a zero closure phase, to estimate the flux and approximate size of VLBI-scale structure and compare with the results of the previous observations.

Circular Gaussian fits to the visibility amplitudes on VLBI baselines are shown in Table 4. The parameters of the best-fit circular Gaussian model agree with values obtained by D12. The compact flux density of 0.98 ± 0.05 Jy is precisely consistent with the D12 value, while the size of 42.9 ± 2.2 μas (corresponding to 5.9 ± 0.2 R_s) is slightly larger but still consistent within 3σ uncertainty. We find no evidence of significant changes in event-horizon-scale structure between the 2009 and 2012 observations.

5. DISCUSSION

5.1. Physical Models for the Structure of 230 GHz Emission

Physically motivated structural models have been proposed for the Schwarzschild-radius-scale structure at 230 GHz in M87 for both jet and disk models (Broderick & Loeb 2009; Dexter et al. 2012; Lu et al. 2014). Although all proposed models predict the existence of a feature at the last photon orbit illuminated by a counter jet and/or accretion disk in the close vicinity of the black hole, there are significant differences between model images. The closure phase is an ideal tool to constrain physically motivated models, since relativistic effects such as gravitational lensing, light bending, and Doppler beaming generally induce asymmetric emission structure in the vicinity of the central black hole, causing the closure phase to be nonzero.

Figure 3 shows images and visibilities of the approaching-jet-dominated models (Broderick & Loeb 2009; Lu et al. 2014), counter-jet-dominated models (J2 in Dexter et al. 2012), and the accretion-disk-dominated models (DJ1 in Dexter et al. 2012). For jet models, 230 GHz emission structure can be categorized into two types. One is the approaching-jet-dominated models, where emission from the approaching jet is predominant at 230 GHz (Broderick & Loeb 2009; Lu et al. 2014). The model images consist of bright blob-like emission from the approaching jet and a weaker crescent or ring-like feature around the last photon orbit illuminated by a counter jet. The emission from the approaching jet dominates the 230 GHz emission regardless of the loading radius of non-thermal particles where leptons are accelerated and the jet starts to be luminous, although the crescent-like feature appears more clearly at smaller particle loading radii (see Figure 3 in Lu et al. 2014). In counter-jet-dominated models, the counter-jet emission is predominant instead of the approaching jet. Such a situation could happen if the bright emission region in the jet is very close to the central black hole (within few R_s), suppressing the approaching jet emission due to gravitational lensing. Photons from the counter jet illuminate the last photon orbit, forming a crescent-like feature. It is worth noting that Dexter et al. (2012) and Lu et al. (2014) have clear differences in their images even at the same particle loading radius of a few R_s, most likely due to differences in magnetic field distribution and also the spatial and energy distribution of non-thermal particles in their models. The accretion disk models are well characterized by a crescent-like or ring-like feature around the last photon orbit. The 230 GHz emission arises in the inner portion of the accretion flow ($r \sim 2.5$ R_s) near the mid-plane.

Measured closure phases on the Hawaii–Arizona–California triangle are consistent with these three models. In Figure 4, we show the model closure phases calculated in the MIT Array Performance Simulator[27] for an approaching-jet-dominated

[27] http://www.haystack.mit.edu/ast/arrays/maps/

Table 2
Closure Phase of M87

Year	DOY	UTC (h)	(m)	Triangle (XYZ)	u_{XY} (Mλ)	v_{XY} (Mλ)	u_{YZ} (Mλ)	v_{YZ} (Mλ)	u_{ZX} (Mλ)	v_{ZX} (Mλ)	Closure Phase (deg)	1σ Error (deg)
2012	81	5	49	SPF	−2336.473	−426.660	1997.198	847.338	339.275	−420.677	3.60	9.98
2012	81	6	3	SPF	−2483.493	−458.173	2113.293	874.212	370.200	−416.039	−3.80	5.05
2012	81	6	26	SPF	−2704.560	−513.928	2286.622	921.497	417.939	−407.569	−6.30	8.67
2012	81	5	49	SPD	−2336.473	−426.660	1997.150	847.284	339.323	−420.624	11.40	11.96
2012	81	6	3	SPD	−2483.493	−458.173	2113.246	874.158	370.247	−415.985	3.50	7.65
2012	81	6	26	SPD	−2704.560	−513.928	2286.577	921.442	417.983	−407.514	−5.10	7.69
2012	81	6	49	SPD	−2898.263	−574.140	2436.772	972.202	461.491	−398.062	−12.80	9.12
2012	81	5	49	SPF	−2336.473	−426.660	1997.198	847.338	339.275	−420.677	2.40	8.38
2012	81	6	3	SPF	−2483.493	−458.173	2113.293	874.212	370.200	−416.039	0.70	5.91
2012	81	6	26	SPF	−2704.560	−513.928	2286.622	921.497	417.939	−407.569	−0.50	5.84
2012	81	6	49	SPF	−2898.263	−574.140	2436.814	972.258	461.449	−398.118	2.70	7.36
2012	81	10	43	SPD	−3029.578	−1284.919	2439.510	1556.894	590.067	−271.975	−0.20	9.21
2012	81	11	6	SPD	−2858.690	−1348.199	2289.791	1607.719	568.899	−259.520	−7.30	9.74
2012	81	11	33	SPD	−2621.320	−1417.355	2084.597	1662.922	536.723	−245.567	3.00	5.07
2012	81	10	43	SPF	−3029.578	−1284.919	2439.508	1556.955	590.070	−272.036	−1.20	8.04
2012	81	11	6	SPF	−2858.690	−1348.199	2289.783	1607.779	568.906	−259.581	−0.60	6.99
2012	81	11	33	SPF	−2621.320	−1417.355	2084.583	1662.983	536.737	−245.628	−0.80	4.59

(This table is available in machine-readable form.)

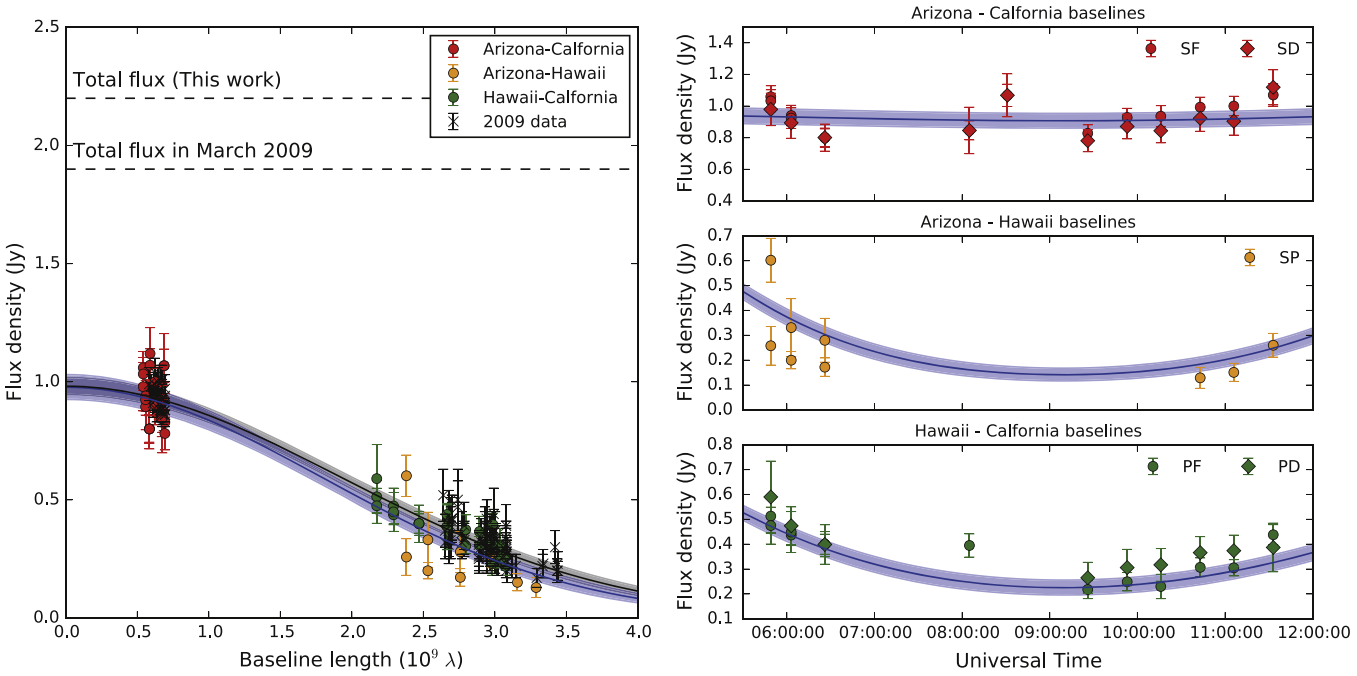

Figure 2. The measured correlated flux density of M87. Circles and crosses indicate the correlated flux density observed in 2012 (this work) and 2009 (Doeleman et al. 2012), respectively. Errors are 1σ. The blue line and light-blue region are best-fit models for the 2012 data and 3σ uncertainties on it, respectively, while the black line and gray region are for the 2009 data. Left panel: correlated flux density as a function of baseline length. Right panels: correlated flux density as a function of Universal Time for each baseline.

model, a counter-jet-dominated model, and an accretion-disk-dominated model in Figure 3. The closure phase of the approaching-jet-dominated model is almost zero. On the other hand, the model closure phases of counter-jet-dominated and accretion-disk-dominated models are systematically smaller than the observed closure phase in the later GST range, but the models and observed closure phases are consistent within a 3σ level. We note that the results for counter-jet-dominated and accretion-disk-dominated models shown in Figure 4 disagree with Figure 9 of Dexter et al. (2012), due to a mistake in Dexter et al. (2012) in constructing the closure phase triangles.

All three models commonly predict small closure phases on the Hawaii–Arizona–California triangle. Visibility phases on the Arizona–California baseline, which barely resolves the source, are nearly zero. The closure phases on current VLBI triangles are almost the same as differences in the visibility phase between long baselines between Hawaii and the US mainland. For the case of the approaching-jet-dominated models, the phase gradient between long baselines is expected to be moderate, particularly at large particle loading radii, since emission is blob-like and fairly symmetric on spatial scales corresponding to the current long baselines. Models with a

Table 3
Gain-corrected Visibility Amplitudes of M87

Year	DOY	UTC (h)	(m)	Baseline	u (Mλ)	v (Mλ)	Correlated Flux Density (Jy)	1σ Error (Jy)
2012	81	5	49	PD	2002.665	845.916	0.59	0.14
2012	81	5	49	PF	2002.599	845.883	0.51	0.07
2012	81	5	49	PF	2002.599	845.883	0.47	0.07
2012	81	5	49	SD	−340.631	421.034	0.98	0.10
2012	81	5	49	SF	−340.698	421.001	1.06	0.07
2012	81	5	49	SF	−340.698	421.001	1.03	0.07
2012	81	5	49	SP	−2343.297	−424.882	0.60	0.09
2012	81	5	49	SP	−2343.297	−424.882	0.26	0.08

(This table is available in its entirety in machine-readable form.)

Table 4
Geometrical Models of M87. Errors are 3σ

Model	Date (Year/DOY)	Compact Flux Density (Jy)	FWHM Size (μas)	χ^2_ν (dof)
2012	2012/81	0.98 ± 0.05	42.9 ± 2.2	2.2 (54)
2009[a]	2009/95–97	0.98 ± 0.04	40.0 ± 1.8	0.6 (102)

Note.
[a] Model obtained from all three days of data in the 2009 observations.

clear crescent-like or ring-like feature generally predict a steep phase gradient around the null amplitude region (see Figure 3), which would be detectable not on the current baselines but on longer ones such as the Hawaii–Mexico baseline.

The observed closure phases cannot distinguish between models with different dominant origin of 230 GHz emission on the current VLBI triangle due to the large errors on the data points. However, future observations with a higher recording rate of 16 Gbps will be able to measure the closure phase with an accuracy within a few degrees at 1 minute integration, which can constrain physical models more precisely. In addition, models can be effectively distinguished by near future observations with additional telescopes such as the Large Millimeter Telescope (LMT) in Mexico or the Atacama Large Millimeter/submillimeter Array (ALMA) in Chile. Differences in closure phases between models become more significant on larger triangles, as shown in the middle and bottom panels of Figure 4.

While all of the physically motivated models are broadly consistent with the currently measured closure phases and amplitudes, they make dramatically different predictions for forthcoming measurements. Models in which the image is dominated by contributions close to the horizon (counter-jet-dominated and accretion-disk-dominated models) exhibit large closure phases on triangles that include the LMT in stark contrast to those dominated by emission further away (approaching-jet-dominated). This extends to the visibility amplitudes: the compact emission models predict nulls on baselines probed by ALMA and the LMT (see Figure 3).

5.2. The Brightness Temperature of the Event-horizon-scale Structure

New VLBI observations of M87 at 230 GHz in 2012 confirm the presence of the event-horizon-scale structure reported in D12. The compact flux density and effective size derived from the circular Gaussian models allow us to estimate the effective brightness temperature of this structure, which is given by (e.g., Akiyama et al. 2013)

$$T_b = \frac{c^2}{2k_B\nu^2}\frac{F}{\pi\phi^2/4\ln 2} \quad (1)$$

$$= 1.44\times10^{10}\,\mathrm{K}\times\left(\frac{\nu}{230\,\mathrm{GHz}}\right)^{-2}\left(\frac{F}{1\,\mathrm{Jy}}\right)\left(\frac{\phi}{40\,\mu\mathrm{as}}\right)^{-2}, \quad (2)$$

where F, ν, and ϕ are the total flux density, observation frequency, and the FWHM size of the circular Gaussian. The effective brightness temperature is $1.42^{+0.11}_{-0.10}\times10^{10}$ K for the 2009 model and $(1.23\pm0.11)\times10^{10}$ K for the 2012 model, where errors are 3σ. These brightness temperatures of $\sim2\times10^{10}$ K are below the upper cutoff in the intrinsic brightness temperature of $\sim10^{11}$ K on the "inverse Compton catastrophe" argument (e.g., Kellermann & Pauliny-Toth 1969; Blandford and Königl 1979; Readhead 1994). Although the 1.3 mm VLBI structure has been poorly constrained, particularly in the N–S direction, possibly inducing additional uncertainties, it is still instructive to discuss the effective brightness temperature and its physical implications for both the jet and accretion disk scenarios.

In the case of the jet scenarios, the brightness temperature would not be highly affected by the Doppler beaming, and then not significantly differ from the intrinsic (i.e., not Doppler-boosted) brightness temperature. The brightness temperature is amplified by a factor of δ for an isotropic blob-like source (e.g., Urry & Padovani 1995). The Doppler factor is 1–3 at a moderate viewing angle of 15°–25° (e.g., Hada et al. 2011) and the Lorentz factor of 1–2 in the inner 10^2 R_s region (e.g., Asada et al. 2014) inferred for the M87 jet.

Interestingly, the 230 GHz brightness temperature is broadly consistent with the peak brightness temperature of $\sim10^9$–10^{10} K at the radio cores at lower frequencies from 1.6 to 86 GHz (e.g., Dodson et al. 2006; Ly et al. 2007; Asada & Nakamura 2012; Hada et al. 2012; Nakamura & Asada 2013) located within $\sim10^2$ R_s from the jet base (Hada et al. 2011). This would provide some implications also for the magnetic field structure of the jet. If we assume that the radio core surface corresponds to the spherical photosphere of the synchrotron self-absorption at each frequency, the magnetic field strength at the radio core can be estimated as (e.g.,

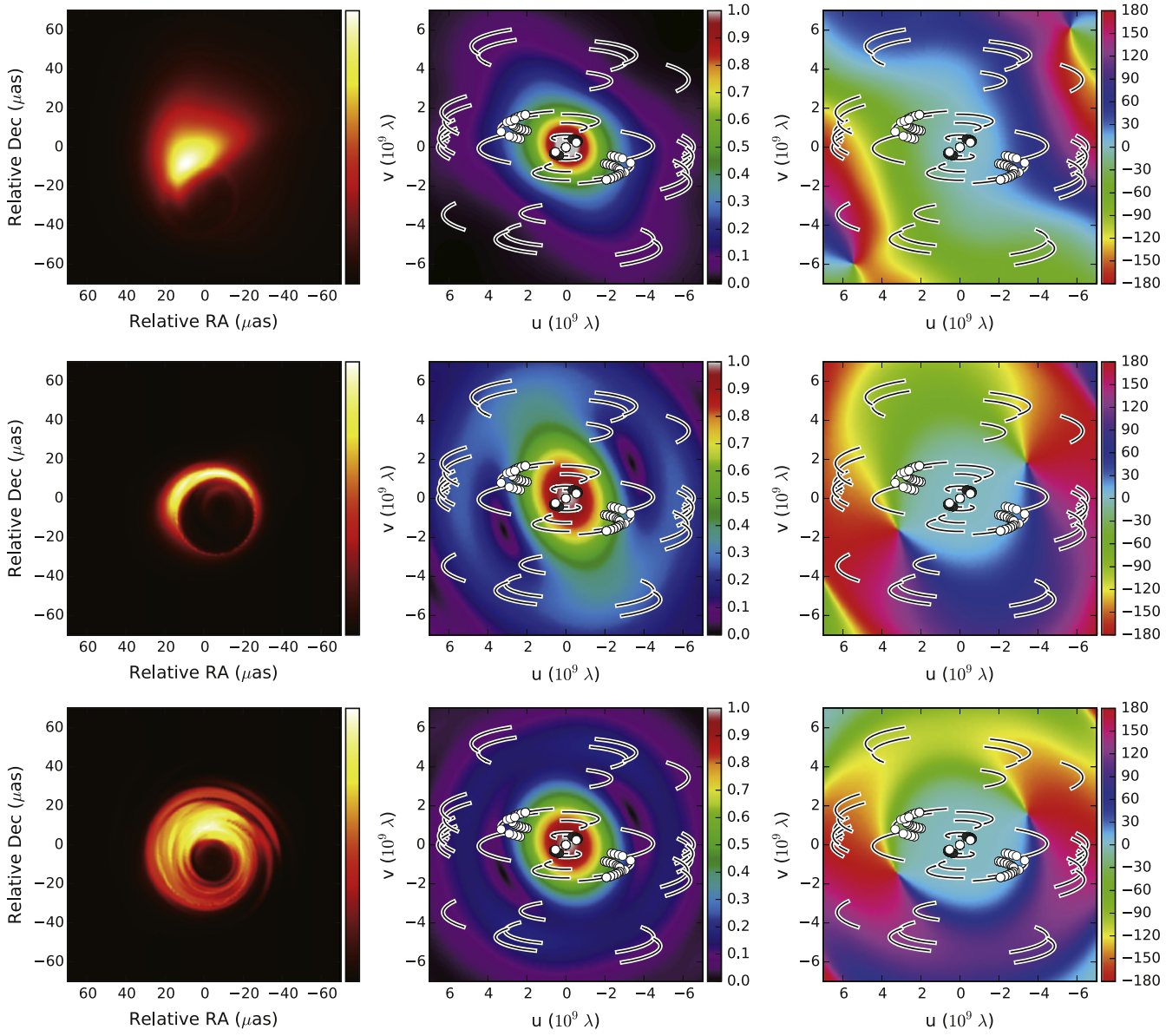

Figure 3. Images (left panels) and distributions of the visibility amplitude (middle panels) and visibility phase (right panels) of the physical models for the structure of 230 GHz emission. The white circle points shows the *uv* coverage of our observations, while the black lines show the *uv* coverage of future observations with current US stations, LMT in Mexico, IRAM 30 m telescope in Spain, PdBI in France, and ALMA/APEX in Chile. Top panels: an approaching-jet-dominated model (Broderick & Loeb 2009; Lu et al. 2014) fitted to 2009 data in Doeleman et al. (2012; Broderick et al. 2015, in preparation). Middle panels: a counter-jet-dominated model (J2) in Dexter et al. (2012) at a position angle of $-70°$ inferred for the large-scale jet. Bottom panels: an accretion-disk-dominated model (DJ1) in Dexter et al. (2012) at a position angle of $-70°$ inferred for the large-scale jet.

Marscher 1983; Hirotani 2005; Kino et al. 2014)

$$B = b(p)\nu^5\phi^4\, F^{-2}\frac{\delta}{1+z} \propto \nu T_b^{-2}\frac{\delta}{1+z}. \quad (3)$$

The constant Doppler factor and brightness temperature give the magnetic field strength as roughly proportional to the observation frequency at the radio core (i.e., $B_{\rm core} \propto \nu_{\rm obs}$). Using the frequency dependence of the radio core position ($r_{\rm core} \propto \nu_{\rm obs}^{-0.59\pm0.09}$; Hada et al. 2011), the magnetic field strength at the radio core is inversely proportional to the distance from the jet base approximately (i.e., $B_{\rm core} \propto r_{\rm core}^{-1}$) in the inner $\sim 10^2\ R_{\rm s}$. This magnetic field profile can be obtained if the transverse (i.e., nearly toroidal) magnetic field dominates on this scale rather than the longitudinal (i.e., nearly poloidal) field along the conical stream with no velocity gradient under the flux frozen-in condition (Blandford and Königl 1979; also see Section 5 in Baum et al. 1997). This profile can also be obtained if the longitudinal (i.e., nearly poloidal) field dominates the transverse (i.e., nearly toroidal) magnetic field along the paraboloidal stream under the flux frozen-in condition, although recent observations favor a conical stream of the jet in the inner $\sim 10^2\ R_{\rm s}$ (Hada et al. 2013).

Even though the above assumptions might not work well for M87, this simple analysis suggests that the dominance of toroidal or poloidal magnetic fields starts to become a major concern on the jet formation in the inner $\sim 10^2\ R_{\rm s}$. Future EHT observations with additional stations and space VLBI observations (e.g., Radio Astron; Kardashev et al. 2013) will provide more detailed structure of the radio core including the profile of

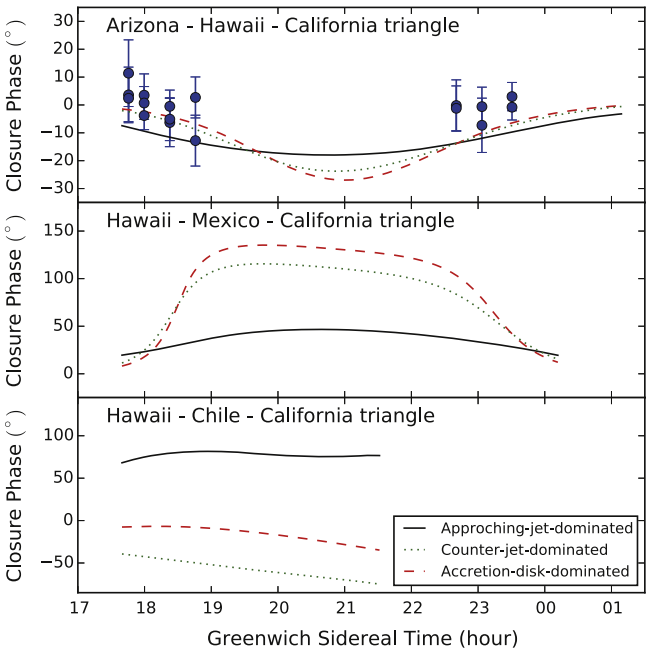

Figure 4. The closure phase of models in Figure 3 as a function of Greenwich Sidereal Time. The black solid line shows an approaching-jet-dominated model (Doeleman et al. 2008; Lu et al. 2014) fitted to 2009 data in Doeleman et al. (2012) (Broderick et al. 2015, in preparation). The red dashed and green dotted lines indicate accretion-disk-dominated and counter-jet-dominated models (DJ1 and J2) in Dexter et al. (2012), respectively, at a position angle of $-70°$ inferred for the large-scale jet. Upper panel: model closure phases on the current VLBI triangle. The circular points are our results shown in Figure 1. Middle panel: model closure phases on a triangle including SMA in Hawaii, CARMA in California, and LMT in Mexico. Lower panel: model closure phases on a triangle including SMA in Hawaii, CARMA in California, and ALMA in Chile.

the stream line, enabling more precise analysis of the magnetic field structure of the relativistic jet in M87.

The measurements of the brightness temperature also give some implications for the energetics of the jet base. The equipartition brightness temperature (Readhead 1994) of the non-thermal plasma with the flux density of ~1 Jy at 230 GHz is $T_{\rm eq} \leqslant 10^{12}$ K, where the equality is given if 230 GHz emission is fully optically thick. This gives the ratio between the internal energy of non-thermal leptons and the magnetic field energy density $U_B/U_e = T_{\rm eq}/T_b \leqslant 10^2$ (Readhead 1994). This implies that, if the 230 GHz emission is dominated by optically thick non-thermal synchrotron emission, the magnetic field energy dominates the internal energy of the non-thermal particles at the jet base. We note that, recently, Kino et al. (2015) performed more careful analysis on the energetics at the jet base, stating that the magnetic field energy is dominant even in the fully optically thin case unless protons are relativistic.

The brightness temperature is broadly consistent with the electron temperature of $\sim 10^{9\text{–}10}$ K as expected for RIAF-type accretion disks (e.g., Manmoto et al. 1997; Narayan et al. 1998; Manmoto 2000; Yuan et al. 2003). The brightness temperature is a factor of ~2–3 smaller than that of Sgr A* with similar size and higher flux density (Doeleman et al. 2008; Fish et al. 2011). If the 230 GHz emission is dominated by thermal synchrotron emission from the accretion disk in both Sgr A* and M87, it seems broadly consistent with a theoretical prediction that a disk with higher accretion rate has a lower electron temperature due to enhanced electron cooling (see Figure 2 in Mahadevan 1997).

5.3. Implications for the VHE Enhancement in 2012 March

Our observations were performed in the middle of the VHE enhancement reported in Beilicke & VERITAS Collaboration (2012) and H14. There are several observational pieces of evidence for the existence of a radio counterpart to the VHE enhancement around our observations. First, the onset of the radio brightening at 22 and 43 GHz occurs simultaneously with the VHE enhancement, indicating that the radio and VHE emission regions are not spatially separated. Since the radio brightening starts ~20–30 days before our observations, 230 GHz emission is also expected to be enhanced at the epoch of our observations. The radio flux measured with the SMA in H14 indeed shows a local maximum in its light curve during our observations, which is consistent with our results showing a radio flux greater than in 2009 April on arcsecond scales when M87 was in a quiescent state (Abramowski et al. 2012). Second, the radio counterpart was not resolved in the radio core in VERA observations, suggesting that the radio counterpart of the 2012 event should exist near the radio core at 43 GHz located at a few tens of Schwarzschild radii downstream from the central black hole and/or the jet base visible at 230 GHz.

The geometrical model (described in Section 4.2) suggests that there are no obvious structural changes on event-horizon scales between 2009 and 2012, despite the increase in the core flux on arcsecond scales. One plausible scenario for explaining the different behavior between event-horizon scales and arcsecond scales is that the structure of the flare component at 230 GHz has extended structure that is resolved out with the current array. The shortest VLBI baseline in our observations, SMT-CARMA, has a length of 600 Mλ. If we consider the Gaussian-like structure for the flaring region with a radio flux of a few ×100 mJy corresponding to the flux increment at the local peak in the 230 GHz light curve of H14, the flaring region should be extended enough to have a correlated flux smaller than the standard deviation on SMT-CARMA baselines of ~90 mJy so that the increment in the radio flux is not significantly detected on those baselines. The minimum FWHM size can be estimated to be ~140 μas ~20 $R_{\rm s}$, which has an HWHM size of ~600 Mλ in the visibility plane. This limitation is consistent with at least two aspects of VHE flares.

First, the 2 months duration of the 2012 VHE event implies that the size of the emission region is $<60\delta$ light days $\sim 0.6\delta$ mas, from causality considerations. Similar constraints of <0.44 mas $\sim 60 R_{\rm s}$ are provided with VERA at 43 GHz in H14, since the flare component was not spatially resolved during their observations. Combining our measurement with these size limits, the size of the VHE emission region during our observations is constrained to be in the tight range of ~0.14–0.44 mas, corresponding to ~20–60 $R_{\rm s}$.

Second, when the size of the emission region is larger than ~20 $R_{\rm s}$, the emitted VHE photons will not be affected by absorption due to the process of photon–photon pair creation ($\gamma\gamma$-absorption). In principle, γ-ray photons with energy E interact most effectively with target photons in the infrared (IR) and optical photon field of energy (e.g., Rieger 2011)

$$\varepsilon(E) \sim \left(\frac{E}{1\ \text{TeV}}\right)^{-1} \text{eV}. \quad (4)$$

Since the 2012 enhancement was detected at ~0.3–5 TeV in the VHE regime (see Beilicke & VERITAS Collaboration 2012), the target photon wavelength is ~0.4–6 μm in the near-infrared (NIR) and optical regimes. The optical depth of γ-rays of energy E for the center of an IR source with a size R and luminosity $L(\varepsilon)$ can be written as (e.g., Neronov & Aharonian 2007)

$$\tau_{\gamma\gamma}(E, R) \approx \frac{\sigma_T}{5}\frac{L(\varepsilon(E))}{4\pi R^2 c\varepsilon}R \approx 0.25\left(\frac{L\{[E/(1\,\mathrm{TeV})]\,\mathrm{eV}\}}{10^{40}\,\mathrm{erg\,s^{-1}}}\right) \times \left(\frac{R}{20\,R_s}\right)^{-1}\left(\frac{E}{5\,\mathrm{TeV}}\right). \quad (5)$$

The NIR and optical luminosity is $L \sim 10^{40}\,\mathrm{erg\,s^{-1}}$ within a few tens of parsecs of the nucleus (e.g., Biretta et al. 1991; Boksenberg et al. 1992). Even in the extreme case that the flaring region accounts for all nucleus emission in the NIR and optical regime, the optical depth is smaller than unity at $E<$ a few TeV, where the enhancement was detected in Beilicke & VERITAS Collaboration (2012), for the size of ~20 R_s. This allows γ-ray photons up to a few TeV to escape from the vicinity of the black hole, explaining why the 2012 event was detectable without introducing a special geometry of emission regions. Note that more careful calculation increases $\tau_{\gamma\gamma}$ by a factor of several (Brodatzki et al. 2011; Broderick & Tchekhovskoy 2015, in preparation), but even in this case the optical depth is smaller than unity for the upper half of the size range (~40–60 R_s).

The scenario limiting the size to a range of ~20–60 R_s during our observations in the middle of the 2012 event can naturally explain our results and other observational results. It is instructive to compare this scenario to the numerous physical models proposed for the VHE emission in M87 (see H14 and Abramowski et al. 2012 for a review). Here, we briefly discuss general implications for the existing VHE models of M87 based on our scenario.

The size of ~20–60 R_s is presumably incompatible with many existing models that assume extremely compact regions of $\lesssim$1–10 R_s, ascribing the VHE emission to particle acceleration in the black hole magnetosphere (e.g., Neronov & Aharonian 2007; Rieger & Aharonian 2008; Levinson & Rieger 2011; Vincent 2014), multiple leptonic blobs in the jet launch/formation region (e.g., Lenain et al. 2008), leptonic models involving a stratified velocity field in the transverse direction (Tavecchio & Ghisellini 2008), mini-jets within the main jet (e.g., Giannios et al. 2010; Cui et al. 2012), and interactions between a red giant star/gas cloud and the jet base (e.g., Barkov et al. 2010, 2012). These models can reasonably explain the very short variable timescale of $\lesssim$1 day in the past three flares in 2005, 2008, and 2010, but are not favored for this particular event in 2012.

Consistency with the size limitation is less clear for models assuming different emission regions or different kinds of emitting particles for radio and VHE emissions, such as hadronic models (e.g., Reimer et al. 2004; Barkov et al. 2010, 2012; Reynoso et al. 2011; Cui et al. 2012; Sahu & Palacios 2013) and some multi-zone leptonic models with a stratified velocity field in radial or transverse directions of the jet by involving the deceleration flow or the spine-layer structure, respectively (Georganopoulos et al. 2005; Tavecchio & Ghisellini 2008). Since the relation between radio and VHE emission has not been well formulated for these models, more detailed predictions particularly on the radio–TeV connection are required for further discussions.

Interestingly, a homogeneous one-zone synchrotron self-Compton (SSC) model (i.e., the standard leptonic model) predicts a comparable source size (~0.1 mas) to our scenario for a broadband spectral energy distribution (SED) in a relatively moderate state (Abdo et al. 2009). It can also naturally explain the radio–VHE connection in H14. The simple leptonic one-zone SSC model seems more plausible than other existing models for M87 to explain some properties such as the size constraint and the radio–VHE connection, but further dedicated modeling for the 2012 event would be required to test consistency with overall observational properties such as the broadband SED, which is not discussed here. Note that leptonic models might be problematic for explaining the hard VHE spectrum, which is common in the previous three VHE flares and the 2012 events, against the Klein–Nishina and γ-ray opacity effects softening the VHE spectrum (see discussions in Tavecchio & Ghisellini 2008).

Our new observations clearly show that short-millimeter VLBI is a useful tool to constrain the size of the radio counterpart, which is a new clue to understanding the VHE activities in M87. In particular, new constraints can be obtained by combining simultaneous EHT observations with measurements of VHE spectra at $\gtrsim$10 TeV highly affected by $\gamma\gamma$ -absorption (see Equation (5)) with the Cherenkov Telescope Array (CTA, Actis et al. 2011). In addition, the complementary dedicated monitoring with lower frequency monitoring on mas and arcsec scales is also important to study details on radio/VHE connections as well as constrain the important physical parameters.

6. SUMMARY

New VLBI observations of M87 at 230 GHz in 2012 confirm the presence of the event-horizon-scale structure reported in D12. We summarize our results as follows:

1. For the first time, we have acquired 230 GHz VLBI interferometric phase information on M87 through measurement of closure phase on the triangle of long baselines. Measured closure phases are consistent with 0°, as expected by physically motivated models for 230 GHz structure such as jet models and accretion disk models. Although our observations cannot currently distinguish models, we show that the future closure phase/amplitude measurements with additional stations and greater sensitivity can effectively distinguish and put a tight constraint on physical models.
2. The brightness temperature of the event-horizon-scale structure is $\sim 1 \times 10^{10}$ K both for previous observations (D12) and for our new observations. This brightness temperature is broadly consistent with that of the radio core at lower frequencies from 1.6 to 86 GHz located in the inner $\sim 10^2$ R_s. We demonstrated a simple analysis assuming that the observed radio core is the photosphere of synchrotron self-absorption. It shows that the constant brightness temperature may give the magnetic field

profile of $B \propto r_{\rm core}^{\sim -1}$ in the inner $\sim 10^2\ R_{\rm s}$, consistent with a prediction of the conical jet with no velocity gradient dominated by the toroidal magnetic field. This indicates that more precise imaging of the radio core with future EHT and space VLBI can address the magnetic field profile in the inner $\sim 10^2\ R_{\rm s}$ crucial for understanding the jet formation.

3. Our observations were conducted in the middle of a VHE enhancement originating in the vicinity of the central black hole. The effective size derived from our data and results of lower frequency observations favor the relatively extended size of VHE emission region of $\sim$20–60 $R_{\rm s}$. This would not favor VHE emission models that predict a compact emission region of $\lesssim 10\ R_{\rm s}$ for this event.

It is clear that future VLBI observations with better sensitivity and additional baseline coverage will be crucial to constrain models of M87 on event-horizon scales.

We would like to thank an anonymous referee for many constructive suggestions to improve the paper. K. Akiyama thanks Dr. Akihiro Doi, Prof. Alan Marscher, Dr. Svetlana Jorstad, and Dr. Jose L. Gómez for fruitful discussions on scientific interpretations. K. Akiyama and K. H. are supported by a Grant-in-Aid for Research Fellows of the Japan Society for the Promotion of Science (JSPS). A. E. B. receives financial support from the Perimeter Institute for Theoretical Physics and the Natural Sciences and Engineering Research Council of Canada through a Discovery Grant. L. L. and G. O.-L. acknowledge the support of DGAPA, UNAM, and CONACyT (México). Event Horizon Telescope work at the MIT Haystack Observatory and the Harvard Smithsonian Center for Astrophysics is supported by grants from the National Science Foundation (NSF) and through an award from the Gordon and Betty Moore Foundation (GMBF-3561). The Arizona Radio Observatory (ARO) is partially supported through the NSF University Radio Observatories (URO) program under grant No. AST 1140030. The Submillimeter Array is a joint project between the Smithsonian Astrophysical Observatory and the Academia Sinica Institute of Astronomy and Astrophysics and is funded by the Smithsonian Institution and the Academia Sinica. Funding for ongoing CARMA development and operations is supported by the NSF and the CARMA partner universities. Event Horizon Telescope work at the Mizusawa VLBI Observatory is financially supported by the MEXT/JSPS KAKENHI Grant Numbers 24540242, 25120007, and 25120008. Research at Perimeter Institute is supported by the Government of Canada through Industry Canada and by the Province of Ontario through the Ministry of Research and Innovation. This work has benefited from open source technology shared by the Collaboration for Astronomy Signal Processing and Electronics Research (CASPER) and from equipment donated by Xilinx Inc.

Facilities: CARMA, JCMT, SMA, SMT

REFERENCES

Abdo, A. A., Ackermann, M., Ajello, M., et al. 2009, ApJ, 707, 55
Abramowski, A., Acero, F., Aharonian, F., et al. 2012, ApJ, 746, 151
Acciari, V. A., Aliu, E., Arlen, T., et al. 2009, Sci, 325, 444
Actis, M., Agnetta, G., Aharonian, F., et al. 2011, ExA, 32, 193
Akiyama, K., Takahashi, R., Honma, M., Oyama, T., & Kobayashi, H. 2013, PASJ, 65, 91
Asada, K., & Nakamura, M. 2012, ApJL, 745, L28
Asada, K., Nakamura, M., Doi, A., Nagai, H., & Inoue, M. 2014, ApJL, 781, L2
Barkov, M. V., Aharonian, F. A., & Bosch-Ramon, V. 2010, ApJ, 724, 1517
Barkov, M. V., Bosch-Ramon, V., & Aharonian, F. A. 2012, ApJ, 755, 170
Baum, S. A., O'Dea, C. P., Giovannini, G., et al. 1997, ApJ, 483, 178
Beilicke, M., & VERITAS Collaboration 2012, AIP Conf. Ser., 1505, 586
Biretta, J. A., Stern, C. P., & Harris, D. E. 1991, AJ, 101, 1632
Blakeslee, J. P., Jordán, A., Mei, S., et al. 2009, ApJ, 694, 556
Blandford, R. D., & Königl, A. 1979, ApJ, 232, 34
Blandford, R. D., & Rees, M. J. 1984, RvMP, 56, 255
Boksenberg, A., Macchetto, F., Albrecht, R., et al. 1992, A&A, 261, 393
Brodatzki, K. A., Pardy, D. J. S., Becker, J. K., & Schlickeiser, R. 2011, ApJ, 736, 98
Broderick, A. E., Fish, V. L., Doeleman, S. S., & Loeb, A. 2011, ApJ, 735, 110
Broderick, A. E., & Loeb, A. 2009, ApJ, 697, 1164
Cui, Y.-D., Yuan, Y.-F., Li, Y.-R., & Wang, J.-M. 2012, ApJ, 746, 177
Dexter, J., Agol, E., Fragile, P. C., & McKinney, J. C. 2010, ApJ, 717, 1092
Dexter, J., McKinney, J. C., & Agol, E. 2012, MNRAS, 421, 1517
Di Matteo, T., Allen, S. W., Fabian, A. C., Wilson, A. S., & Young, A. J. 2003, ApJ, 582, 133
Dodson, R., Edwards, P. G., & Hirabayashi, H. 2006, PASJ, 58, 243
Doeleman, S. S., Fish, V. L., Broderick, A. E., Loeb, A., & Rogers, A. E. E. 2009, ApJ, 695, 59
Doeleman, S. S., Fish, V. L., Schenck, D. E., et al. 2012, Sci, 338, 355
Doeleman, S. S., Shen, Z.-Q., Rogers, A. E. E., et al. 2001, AJ, 121, 2610
Doeleman, S. S., Weintroub, J., Rogers, A. E. E., et al. 2008, Natur, 455, 78
Doi, A., Hada, K., Nagai, H., et al. 2013, European Physical Journal Web of Conferences, 61, 8008
Fish, V., Alef, W., Anderson, J., et al. 2013, arXiv:1309.3519
Fish, V. L., Doeleman, S. S., Beaudoin, C., et al. 2011, ApJL, 727, L36
Gebhardt, K., Adams, J., Richstone, D., et al. 2011, ApJ, 729, 119
Georganopoulos, M., Perlman, E. S., & Kazanas, D. 2005, ApJL, 634, L33
Giannios, D., Uzdensky, D. A., & Begelman, M. C. 2010, MNRAS, 402, 1649
Gracia, J., Vlahakis, N., Agudo, I., Tsinganos, K., & Bogovalov, S. V. 2009, ApJ, 695, 503
Hada, K., Doi, A., Kino, M., et al. 2011, Natur, 477, 185
Hada, K., Giroletti, M., Kino, M., et al. 2014, ApJ, 788, 165
Hada, K., Kino, M., Doi, A., et al. 2013, ApJ, 775, 70
Hada, K., Kino, M., Nagai, H., et al. 2012, ApJ, 760, 52
Hirotani, K. 2005, ApJ, 619, 73
Ho, P. T. P., Moran, J. M., & Lo, K. Y. 2004, ApJL, 616, L1
Honma, M., Akiyama, K., Ikeda, S., et al. 2014, arXiv:1407.2422
Inoue, M., Algaba-Marcos, J. C., Asada, K., et al. 2014, arXiv:1407.2450
Kardashev, N. S., Khartov, V. V., Abramov, V. V., et al. 2013, ARep, 57, 153
Kellermann, K. I., & Pauliny-Toth, I. I. K. 1969, ApJL, 155, L71
Kino, M., Takahara, F., Hada, K., & Doi, A. 2014, ApJ, 786, 5
Kino, M., Takahara, F., Hada, K., et al. 2015, ApJ, 803, 30
Kino, M., Takahara, F., & Kusunose, M. 2002, ApJ, 564, 97
Komissarov, S. S., Barkov, M. V., Vlahakis, N., & Knigl, A. 2007, MNRAS, 380, 51
Königl, A. 1981, ApJ, 243, 700
Kovalev, Y. Y., Lister, M. L., Homan, D. C., & Kellermann, K. I. 2007, ApJL, 668, L27
Kuo, C. Y., Asada, K., Rao, R., et al. 2014, ApJL, 783, L33
Lenain, J.-P., Boisson, C., Sol, H., & Katarzyński, K. 2008, A&A, 478, 111
Levinson, A., & Rieger, F. 2011, ApJ, 730, 123
Lu, R.-S., Broderick, A. E., Baron, F., et al. 2014, ApJ, 788, 120
Lu, R.-S., Fish, V. L., Akiyama, K., et al. 2013, ApJ, 772, 13
Lu, R.-S., Fish, V. L., Weintroub, J., et al. 2012, ApJL, 757, L14
Ly, C., Walker, R. C., & Junor, W. 2007, ApJ, 660, 200
Macchetto, F., Marconi, A., Axon, D. J., et al. 1997, ApJ, 489, 579
Mahadevan, R. 1997, ApJ, 477, 585
Manmoto, T. 2000, ApJ, 534, 734
Manmoto, T., Mineshige, S., & Kusunose, M. 1997, ApJ, 489, 791
Marscher, A. P. 1983, ApJ, 264, 296
Martin, R. N., & Baars, J. W. M. 1986, BAAS, 18, 943
McKinney, J. C. 2006, MNRAS, 368, 1561
Mościbrodzka, M., Gammie, C. F., Dolence, J. C., Shiokawa, H., & Leung, P. K. 2009, ApJ, 706, 497
Mościbrodzka, M., Shiokawa, H., Gammie, C. F., & Dolence, J. C. 2012, ApJL, 752, L1
Mundy, L. G., & Scott, S. L. 2000, in ASP Conf. Ser. 217, Imaging at Radio through Submillimeter Wavelengths, ed. J. G. Mangum & S. J. E. Radford (San Francisco, CA: ASP), 235
Nagakura, H., & Takahashi, R. 2010, ApJ, 711, 222

Nakamura, M., & Asada, K. 2013, ApJ, 775, 118
Narayan, R., Mahadevan, R., Grindlay, J. E., Popham, R. G., & Gammie, C. 1998, ApJ, 492, 554
Narayan, R., & Yi, I. 1995, ApJ, 444, 231
Neronov, A., & Aharonian, F. A. 2007, ApJ, 671, 85
Newport, R. W. 1986, JBIS, 39, 211
Readhead, A. C. S. 1994, ApJ, 426, 51
Reid, M. J., Biretta, J. A., Junor, W., Muxlow, T. W. B., & Spencer, R. E. 1989, ApJ, 336, 112
Reimer, A., Protheroe, R. J., & Donea, A.-C. 2004, A&A, 419, 89
Reynolds, C. S., Di Matteo, T., Fabian, A. C., Hwang, U., & Canizares, C. R. 1996, MNRAS, 283, L111
Reynoso, M. M., Medina, M. C., & Romero, G. E. 2011, A&A, 531, A30
Rieger, F. M. 2011, IJMPD, 20, 1547
Rieger, F. M., & Aharonian, F. A. 2008, IJMPD, 17, 1569
Rogers, A. E. E., Doeleman, S. S., & Moran, J. M. 1995, AJ, 109, 1391
Sahu, S., & Palacios, E. 2013, arXiv:1310.1381
Takahashi, R., & Mineshige, S. 2011, ApJ, 729, 86
Tavecchio, F., & Ghisellini, G. 2008, MNRAS, 385, L98
Urry, C. M., & Padovani, P. 1995, PASP, 107, 803
Vincent, S. 2014, IJMPS, 28, 60189
Walsh, J. L., Barth, A. J., Ho, L. C., & Sarzi, M. 2013, ApJ, 770, 86
Whysong, D., & Antonucci, R. 2004, ApJ, 602, 116
Yuan, F., & Narayan, R. 2014, arXiv, arXiv:1401.0586
Yuan, F., Quataert, E., & Narayan, R. 2003, ApJ, 598, 301
Zakamska, N. L., Begelman, M. C., & Blandford, R. D. 2008, ApJ, 679, 990